CDF/ANAL/CDF/CDFR/2050[1]

Measurement of $\bar{p}p$ Single Diffraction Dissociation at $\sqrt{s}$=546 and 1800 GeV

S. Belforte, G. Chiarelli, P. Giromini, K. Goulianos,
S. Miscetti and R. Paoletti

April 22, 1993

Abstract

We report a measurement of the diffraction dissociation differential cross section $d^2\sigma_{sd}/dM^2dt$ for $\bar{p}p \rightarrow \bar{p}$ X at $\sqrt{s}$=546 and 1800 GeV, $M^2/s < 0.2$ and $0 \leq -t \leq 0.4$ GeV^2. Our results are compared to theoretical predictions and to extrapolations from experimental results at lower energies.

The reaction $\bar{p}p \rightarrow \bar{p}$ X was studied at the Tevatron at c.m.s. energies $\sqrt{s}$ =546 and 1800 GeV by detecting the recoil antiproton and a large fraction of the products of the system X. The double differential cross-section $d^2\sigma/dM^2dt$ was measured at $M^2/s < 0.2$ and $0 \leq -t \leq 0.4$ GeV^2. The same experimental apparatus was also used for the simultaneous measurement of the elastic scattering and the total cross-section, reported in the preceding [1] and following [2] papers.

[1]to be submitted to Phys. Rev. D

I. EXPERIMENTAL METHOD

The recoil antiproton was observed by a magnetic spectrometer composed of two arms in the horizontal plane of the machine : arm-0 on the outside and arm-1 on the inside of the Tevatron beam orbit. In each arm, the $\bar{p}$ trajectory was measured at three different z-points along the beam line by detectors S1, S2 and S3 placed inside beam pipe sections with variable aperture (Fig. 1 of [1]). Each detector consisted of four planes of drift chambers, a silicon detector and two trigger counters.

The charged particles from the proton fragmentation were observed by the vertex detectors S4, FTB, VTPC, FTF and S5 (Fig.1 of [2]). The VTPC [3], a system of eight time projection chambers around the beam pipe, covered the pseudo-rapidity region $|\eta| < 3.5$. In addition, four telescopes of drift wire chambers, symmetrically placed on the left side (FTB, S4) and the right side (FTF, S5) of the interaction region, covered the region $3.8 < |\eta| < 6.7$. Each telescope was backed by TOF and trigger counters ($3.2 < |\eta| < 6.7$).

The trigger required a particle through detectors S1 and S2 in coincidence with at least one particle in the region $3.2 < \eta < 6.7$ on the proton fragmentation side.

The recoil antiproton was deflected in the horizontal (x-z) plane by the Tevatron dipole and quadrupole magnets. Its momentum p and recoil angle θ were calculated from the (x_1,y_1) and (x_2,y_2) positions measured by S1 and S2, using the well known values of the machine lattice transfer matrices [1] and assuming x=y=0 at z=0. The projected positions (x_{3proj}, y_{3proj}) in S3 were also evaluated and used in making fiducial cuts.

The momentum resolution, $\sigma_p(p)$, at $p_0 = \sqrt{s}/2$ was determined by reconstructing the antiproton momentum in a sample of elastic events. As shown in Fig. 1, the measured

$\sigma_p(p_0)/p_0$ is about 0.2% at both c.m.s. energies in agreement with our simulation. For $p<p_0$, the simulation shows that at $\sqrt{s} = 546$, where data were taken with the low-β quadrupoles almost at full power [1], $\sigma_p(p)=0.5\ p/p_0(1\text{-}4(p_0\text{-}p)/p_0)$ GeV. In the high-β runs at $\sqrt{s} = 1800$ [1], $\sigma_p(p)=2.5\ p/p_0$ GeV.

The momentum and angle of the recoil antiproton were used to calculate:

the Feynman scaling variable $x=p/p_0$,

the system X mass $M^2 = (1-x)s$ and

the four-momentum transfer $t = m^2(1-x)^2/x+2p_0^2x(1-\cos\theta)$, where m is the proton mass.

The simulated acceptance $A(x,t)$ of the recoil spectrometer is shown in Fig. 2.

Given a functional form for $d^2\sigma/dM^2dt$ (see section IV), we fitted to the data the product $d^2\sigma/dM^2dt \cdot A(x,t) \cdot E(M^2)$ in the region where $A(x,t)$ is larger than 0.02; $E(M^2)$ is the efficiency for triggering and reconstructing the vertex for a given M . The total single diffraction cross section was obtained by integrating $d^2\sigma_{sd}/dM^2dt$ over the full momentum transfer in the diffraction region [4, 5] 1.4 GeV$^2 < M^2 < 0.15\ s$.

II. DATA REDUCTION

From a total of 15272 events collected in one run at $\sqrt{s}$=546 and 73480 events in two different runs at $\sqrt{s}$=1800, we selected 4873 and 3674 events, respectively (see Table 1). Events were rejected when halo particles in time with the incoming beams

were detected by our time of flight counters (TOF FILTER) or if the VTPC detected particle showers originating upstream of the interaction region (VTPC FILTER). The losses due to TOF and VTPC filters were evaluated and are listed in Table 1. Events were further rejected if S1 and S2 in the triggering arm had more than one hit and S1 or S2 in the opposite arm had more than 4 hits (HITS CUT). Otherwise, multi-hit events (1% of the total) were retained . Events were not accepted if we were unable to reconstruct a track segment in the S1 or S2 detectors (S1*S2 TRACK CUT). The last two requirements do not cause appreciable inefficiencies, as shown by the analysis of our elastic events [1].

In accordance with our elastic scattering analysis, in order to avoid edge effects, we removed events which lay within 0.05 cm of detector boundaries (FIDUCIAL CUT 1). When the projection of the measured antiproton trajectory was within the S3 detectors, the differences between the measured (x_3,y_3) coordinates and the projected coordinates were required to be within three times the detector spatial resolution (FIDUCIAL CUT 2). Since the machine dipoles bend the recoil antiprotons towards the inside of the beam orbit, S3 is always hit when events trigger arm-0, while S3 can be missed by events triggering arm-1. Fig. 3 shows scatter plots of x_2 vs. x_3 for all the accepted events at $\sqrt{s} = 546$, for the events which also pass the fiducial cuts and for simulated events with all cuts. Negative values of x_2 correspond to $\bar{p}$'s detected in arm-1, while x_2 is positive if $\bar{p}$'s are detected in arm-0. Elastically scattered $\bar{p}$'s would cluster along the solid line in Fig. 3a. For a given x_3, i.e. a given recoil angle θ, decreasing values of x_2 correspond to increasingly lower antiproton momenta and higher diffractive masses. In arm-0, events above the elastic line are out of the spectrometer acceptance for particles originating at the interaction region and are due to antiprotons in the beam

halo that have small θ-angle but are sufficiently away from the beam-center as to be detected. In arm-1, such halo particles can fake diffractive events. Similar plots for the first $\sqrt{s} = 1800$ run are shown in Fig. 4. Here, due to a different optical beam tune [1], halo particles fake diffractive events in arm-0, while they remain outside the acceptance in arm-1. To reduce the arm-0 halo background at $\sqrt{s} = 1800$, we limited the arm-0 acceptance in the x_2-x_3 plane as shown in Figs. 4b and 4c. Similarly, to reduce the arm-1 background at $\sqrt{s} = 546$, we accepted only events in which S3 was also hit (FIDUCIAL CUT 3). The losses due to all fiducial cuts ($< 1\%$) were included in the acceptance calculation.

The requirements and cuts listed above removed most of the halo background. The residual halo contamination was evaluated by examining the distribution of $(x_3\text{-}x_{3proj})$ after having applied all cuts listed in Table 1 except FIDUCIAL CUT 2. Fig. 5a shows the distributions of $(x_3\text{-}x_{3proj})$ in arm-1 for data and simulation at $\sqrt{s} = 546$. The background contribution was estimated to be $\ll 1\%$. Similar distributions are shown in Fig. 5b for arm-0 data from the first run at $\sqrt{s}$=1800. The background is clearly visible as a shoulder on the right hand side of the distribution. This background was attributed to halo particles. A good fraction of these halo particles could be tagged, as they were also observed by the S6 and S7 detectors of the elastic scattering spectrometer upstream of the interaction region. The distribution of $(x_3\text{-}x_{3proj})$ for the tagged halo events is shown in Fig. 5b, normalized to the region $(x_3\text{-}x_{3proj}) > 0.2$ cm where no good events are expected from the simulation. From this distribution, the background contamination within all fiducial cuts in this run was estimated to be $5\pm1\%$ in arm-0 and $1.8\pm0.4\%$ in all events. As shown, the data are accurately reproduced by the sum of the normalized background and a complementary amount of simulated events. The

5% background contamination was statistically removed by subtracting from the data the same amount of tagged halo events passing all cuts. The background in the second run at $\sqrt{s} = 1800$ was $\ll 1\%$.

Finally, events were rejected in which no vertex was found (VERTEX CUT). Fig. 6 and Fig. 7 show vertex z-distributions as reconstructed from data and simulation using the VTPC or FTF+S5 at $\sqrt{s} = 546$ and $\sqrt{s}$=1800. One track is enough to reconstruct the vertex by determining its z-position at which x=y=0. The excellent agreement between data and simulation shows that the background contamination in our final sample is negligible.

Table 1 summarizes the event flow through all cuts and requirements leading to the final sample of events. Corrections for nuclear interactions in the spectrometer detectors, as measured in Ref. [1] and listed in Table 1, were applied. The final numbers of events must be multiplied by the prescaling factor of the single diffractive trigger and by a factor of two to account for the dissociation of the antiproton, assumed to be the same as that of the proton.

III. MONTE CARLO SIMULATION

The trigger and vertex finding efficiency, E(M^2), was determined by simulation. Simulation details are given in Appendix B of Ref.[2]. In our simulation, single diffraction was generated in the mass range 1.4 GeV^2 $< M^2 <$ 0.15 s with a distribution

$$d^2\sigma_{sd}/dM^2dt = A\frac{b(M)}{M^2}e^{b(M)t} \qquad (1)$$

where $b(M) = \frac{2}{3}b_{el}(1 + \frac{0.04}{(M-\sqrt{2})^2+0.02})$ and b_{el} is the elastic slope [1].

The known resonances in the region $M^2 < 6$ GeV^2 were also generated. Their integrated cross section is equal to the integral of (1) below 6 GeV^2. For a given mass M of the system X, the average generated total multiplicity is

$$n = 1.5\,(2 + 0.13\,ln(M-m)^2 + 0.175\,ln^2(M-m)^2).$$

The multiplicity of each event was distributed according to the prescription given in Ref.[6]. For multiplicities larger than three, particle four-momenta were generated as described in Ref.[2]. Two and three body decays were generated according to exact phase space, assuming that the nucleon angular distribution in the rest frame of M is given by $(1 + \cos\theta^{*2})$. Decay products were then boosted into the laboratory frame and tracked through the entire CDF detector [3], allowing for secondary decays, conversions and interactions in the beam pipe and all detector elements.

The resulting charged particle pseudo-rapidity distributions as seen by the VTPC, FTF and S5 detectors are compared to the data at $\sqrt{s} = 546$ in Fig. 8. The same comparison at $\sqrt{s} = 1800$ is shown in Fig. 9. The agreement between data and simulation is impressive, especially in the trigger region of $\eta > 3.2$. As one can see in Fig. 8b, the simulation might require only a little tuning at the tail of the η-distribution, measured by the VTPC for events with $x > 0.95$. However, such tuning would not alter our efficiency estimates.

The total number of measured tracks in all detectors compares well with the simulation at both energies (Fig. 10). The average number of tracks as a function of $(1-x)$ in the data and simulation is shown in Fig. 11. One may notice the partial agreement between data and simulation. Several effects contribute: the single diffraction differential cross section $d\sigma_{sd}/dx$ used in the simulation is slightly different from the

result of our fit to the data and, as discussed in section V, the data contain an appreciable non-diffractive contribution; in addition, the simulation accounts for secondary interactions, which appreciably increase the generated event multiplicity. For all these reasons, further work is needed to extract from the data accurate results on average multiplicities and angular distributions of diffractive events. However, for the purpose of estimating $E(M^2)$, the small differences between the observed and measured multiplicity distributions, particularly at large multiplicities, are not important.

Trigger and vertex-reconstruction inefficiencies on the diffractive cluster side are only due to two and three body decays, which, as mentioned above, are generated with exact phase space. For all $M^2 \leq 6$ GeV^2 (where 2 and 3 body decays dominate) the total efficiency is 68% and 40% at $\sqrt{s} = 546$ and $\sqrt{s} = 1800$, respectively. By changing the known ratio of the 2 body to 3 body decay fractions by a factor two, the efficiency at both energies changes only by 1%. As diffractive masses become larger, the fraction of 2 and 3 body decay channels decreases and decay angles with respect to the proton increase, so that the efficiency $E(M^2)$ increases with M^2. The efficiency at our two energies is shown in Fig. 12 as a function of $(1\text{-}x)$ for $(1\text{-}x) \leq 0.0001$. The detector is fully efficient for events with $x < 0.998$; for $x > 0.998$, convoluting $E(x)$ with $d\sigma_{sd}/dx$ from our best fit, we obtain at both energies an integrated efficiency

$$\int_{0.998}^{1} \frac{d\sigma_{sd}}{dx} E(x) dx \Big/ \int_{0.998}^{1} \frac{d\sigma_{sd}}{dx} dx \simeq 0.8$$

IV. DATA FITTING

We fitted to our data the standard triple-Pomeron Regge formula for single diffraction

dissociation [7, 8, 9]

$$s\, d^2\sigma_{sd}/dtdM^2 = G(t)(s/s_0)^{\alpha_p(0)-1}(s/M^2)^{2\alpha_p(t)-\alpha_p(0)} \tag{2}$$

where we lumped into $G(t)$ all four Regge couplings and the signature factors. Following tradition, we assumed a linear Pomeron trajectory $\alpha_p(t) = 1 + \epsilon + \alpha' t$, treating ϵ as a fit free parameter and assuming $\alpha' = 0.25$ GeV^{-2} [1, 4, 5, 9, 10, 11, 12] . At each energy, $G(t) \cdot (s/s_0)^{\epsilon}$ was parametrized as $G(0) \cdot (s/s_0)^{\epsilon} \cdot e^{b_0 t} = D \cdot e^{b_0 t}$. Formula (2) can then be written as

$$s\, d^2\sigma_{sd}/dtdM^2 = D \cdot e^{(b_0 + 2\alpha' ln(s/M^2))t} \cdot (s/M^2)^{1+\epsilon} \tag{3}$$

In order to account for non-diffractive contributions at $x \geq 0.8$, we added to formula (3) the empirical term [4] (see Appendix C of Ref.[2])

$$d^2\sigma_{nd}/dtdx = I \cdot (1-x)^{\gamma} \cdot e^{b' t} \tag{4}$$

The sum (3)+(4), smeared by the detector resolution and the beam profile and multiplied by the acceptance A(M^2,t), by the total integrated luminosity L and by E(M^2), was fitted to the data using a maximum likelihood method to determine $G(0) \cdot (s/s_0)^{\epsilon} \cdot L = D \cdot L$, b_0, ϵ, $I \cdot L$, b' and γ .

V. RESULTS

Fit results are listed in Table 2 and fit parameter correlation coefficients are given in Table 3. Data and fits are compared in Figs. 13 and 14. In our fits, we assumed

α'=0.25 GeV^{-2} in order to reduce the number of free parameters. A change in α' by $\pm$0.1 GeV^{-2} results in a change in σ_{sd} of only $\pm$0.1%. At the same time, ϵ changes by $\delta\epsilon = \pm 0.013$ and b_0 by $\delta b_0 = \mp 1.5$ GeV^{-2} . These values $\delta\epsilon$ and δb_0 represent systematic errors to be added to the fit statistical errors for ϵ and b_0 at both energies.

A. t-Dependence

The standard Regge form of the diffractive slope

$$b = b_0 + 0.5\, GeV^{-2} \cdot \ln(s/M^2) \tag{5}$$

fits well our data at each energy. However, our fits yielded $b_0 = 8.7 \pm 0.6$ GeV^{-2} at $\sqrt{s}$=546 and $b_0 = 5.5 \pm 0.6$ GeV^{-2} at $\sqrt{s}$=1800. This difference in the b_0's may be a consequence of the fact that *low masses* ($M^2 \leq$6 GeV^2), which represent a large fraction of the resolution-dominated diffractive peak at $x \simeq 1$ (Figs. 13a and 14a), have slopes steeper than those given by eq.(5). At $M^2 \simeq 2$ GeV^2, the slopes derived from our fits are b=14.6 and 12.6 GeV^{-2} at $\sqrt{s}$=546 and 1800, respectively. These values are smaller than the elastic slopes b_{el}=15.35 and 17.0 GeV^{-2} at the two energies, whence at lower (fixed target) energies the *low mass* diffractive slopes were found to be larger than the elastic ones [13, 14].

The region of $\pm 2\sigma_x$ around x=1 contains 68% of all diffractive events at 546 and 83% at 1800 GeV. While the parameter ϵ is determined primarily by the remaining 32% (20%) of the events, the slope b_0 is determined mainly by the events in this $4\sigma_x$ region; of these events, 27% (13%) are estimated from our fit to be due to *low masses*. The difference in the b_0 values obtained at the two energies could be explained as the result

of the different contribution of the *low masses* to the diffractive peak at $x \simeq 1$, if one assumed the average slope in the *low mass* region to be about 20 GeV^{-2}.

Since the D value in our fits is strongly correlated to b_0, the result for σ_{sd} is not very sensitive to the value of b_0 . In fits where b_0 was varied by $\pm$ 2 GeV^{-2} or where the slope b was set to be 20 GeV^{-2} at *low masses* (see section V. D), the result for σ_{sd} did not change by more than 1%.

B. M^2-Dependence

The parameter ϵ, which measures the deviation of the differential cross section $d\sigma_{sd}/dM^2$ from $1/M^2$ dependence, was determined to be $\epsilon = 0.155^{+0.014}_{-0.013}$ at $\sqrt{s} = 546$ and $\epsilon = 0.116^{+0.034}_{-0.026}$ at $\sqrt{s} = 1800$. Theoretically, $1 + \epsilon$ can be interpreted as the intercept of a supercritical Pomeron, assuming that only the triple-Pomeron diagram contributes to diffraction dissociation and neglecting screening effects [15]. Under the same theoretical assumptions, the total cross section, σ_T, behaves as $s^{\alpha_P(0)-1} = s^{\epsilon}$. From our measurements of σ_T at $\sqrt{s}$=546 and $\sqrt{s}$=1800 [2], we derive $\epsilon = 0.115 \pm 0.013$, which is in general agreement with the above results.

The ratio of the ϵ measured in single diffraction at $\sqrt{s}$=546 to that derived from the total cross section rise is 1.35 ± 0.18. In view of the correlations between ϵ and the other fit parameters, this 2σ deviation from unity may not be as significant as statistics would indicate; however, it may be taken as mildly suggesting that screening corrections are needed [15].

C. s-Dependence

According to equation (3), the total diffractive cross section is given by

$$\sigma_{sd} = G(0)(s/s_0)^{\epsilon} s^{\epsilon} \int_{1.4GeV^2}^{0.15s} \frac{M^{-2(1+\epsilon)}}{b_0 + 0.5ln(s/M^2)} dM^2 \qquad (6)$$

Using $\epsilon = 0.115 \pm 0.013$ (from the rise of σ_T) and $b_0 = 7.1$ GeV^{-2} (the average at our two energies), the value of σ_{sd}=7.8±0.3 mb measured at $\sqrt{s}$=546 extrapolates to $\sigma_{sd} = 13.5 \pm 0.7$ at $\sqrt{s}$=1800, where we measure $\sigma_{sd} = 8.8 \pm 0.7$ mb. The ratio of the measured σ_{sd} at $\sqrt{s}$=1800 to that obtained by extrapolation from $\sqrt{s}$=546 is 0.65±0.06, clearly indicating that large screening corrections have to be introduced in order to save the traditional supercritical Pomeron model.

Direct comparison of our results with experiments at lower energies is made difficult by the fact that the data in these experiments were not fitted with exactly the same function as ours. To compare our results to lower energy data, we fitted the form (3)+(4) to published data at $\sqrt{s}$ =20 GeV [16], supplemented by points measured in the region $x \leq 0.95$ at $\sqrt{s}$=23.5 GeV [17]. Since t-distributions as a function of M^2 are not available from these experiments, we used in the fits $b = 4.5 + 0.5 \cdot ln(s/M^2)$ GeV^{-2} for single diffraction and $b' = 6.5$ GeV^{-2} for the inelastic contribution, consistent with the slopes given in [16, 17] and with other measurements at the ISR [18].

Our fit to the low energy data is shown in Fig. 15. The fit results are listed below :

σ_{sd}(mb)	D (mb/GeV^2)	ϵ	σ_{nd} (mb)	I (mb/GeV^2)	γ
4.9±0.3	4.5±2.4	0.2±0.12	1.7±0.3	642±289	0.83±0.27

The cross section values listed above are for $x \geq 0.85$. We estimate that, due to the uncertainty in the slopes [18], a 10% systematic error should be attached to these cross sections.

The measured $\sigma_{sd} = 4.9 \pm 0.55$ mb at $\sqrt{s}$=20 GeV is 4.5 times larger than the value $\sigma_{sd} = 1.1 \pm 0.1$ mb obtained by extrapolating our measured value at $\sqrt{s}$=546 down to $\sqrt{s}$=20 using eq.(6). It is interesting to note that the factor 4.5 is almost entirely due to the term $s^{2\epsilon}$ in eq.(6).

Theoretical approaches [15, 19, 20], which describe single diffraction dissociation as a multi-Pomeron exchange with the eikonal formalism, predict a rather flat s dependence of σ_{sd} while breaking the (s/M^2) scaling of $s\, d^2\sigma_{sd}/dM^2dt$. A useful representation of eq.(6) for testing such models is

$$\sigma_{sd} = K \cdot (s/s_0)^{\delta} \int_{1.4GeV^2}^{0.15s} \frac{(M/m_0)^{-2(1+\epsilon)}}{b_0 + 0.5ln(s/M^2)} dM^2 \qquad (7)$$

Treating δ as a free parameter, we determined its value from a simultaneous fit to the diffractive cross sections σ_{sd} at $\sqrt{s}$=20, 546 and 1800 GeV. Using the average value b_0=6.2 GeV^{-2} at all three energies and assuming a common ϵ=0.15, we obtained $\delta = 0.03 \pm 0.03$; using the measured value of ϵ at each energy, $\delta = -0.03 \pm 0.03$.

D. Comparison with other experiments

At $\sqrt{s}$=546, our total inelastic cross section in the region $x \geq 0.85$ is 9.3$\pm$0.25 mb, of which σ_{sd} accounts for 7.8$\pm$0.3 mb. At the same energy, the UA4 experiment [21] obtained the value $\sigma_{sd} = 9.4 \pm 0.7$ mb for $x \geq 0.95$, corresponding to $\sigma_{sd} = 10.4 \pm 0.8$

mb for $x \geq 0.85$.

The discrepancy between the two results for σ_{sd} can be understood in terms of the way the data were fitted in the two experiments. Motivated by lower energy experiments [13], UA4 fitted to the data the expression

$$d^2\sigma_{sd}/dtdM^2 = \frac{D}{M^2}e^{b_0 t} \tag{8}$$

which is the same as (3) when ϵ=0 and α'=0. The parameter D was allowed to be different in the resonance region of $M^2 < 16$ GeV^2 and non-diffractive contributions, which account for most of the discrepancy, were incorporated into σ_{sd}. The fit yielded $b_0 = 8.0 \pm 0.1$ GeV^{-2} and a discontinuity in the mass spectrum: $D/b_0 = 0.93 \pm 0.09$ mb for $M^2 > 16$ GeV^2 (corresponding to $\sigma_{sd}[M^2 > 16$ GeV$^2]$=7.4$\pm$0.5 mb) and $D/b_0 = 1.23 \pm 0.26$ mb in the region $M^2 \leq 16$ GeV^2 (corresponding to $\sigma_{sd}[M^2 \leq 16$ GeV$^2]$=3.0$\pm$0.6 mb).

Following the same approach, we also fitted (8) to our data, allowing D and b_0 to be different at $M^2 < 16$ GeV^2. However, because of our good mass resolution in the high mass region compared to that of UA4, in order to obtain a reasonable fit at all masses we were forced to add to (8) the term (4), which accounts for non diffractive contributions. This fit yielded a total integrated cross section in the mass region 1.4 GeV$^2 < M^2 < 0.15\ s$ of 11.3$\pm$0.5 mb and, as expected, a larger discontinuity in the mass spectrum. The results of the fit are listed below:

σ_{sd} (mb)	$\sigma_{sd}[M^2 > 16\ \mathrm{GeV}^2]$ (mb)	$\sigma_{sd}[M^2 \leq 16\ \mathrm{GeV}^2]$ (mb)	σ_{nd} (mb)	
10.3±0.4	5.4±0.3	4.9±0.3	1.0±0.6	
	$b_0[M^2 > 16\ \mathrm{GeV}^2](\mathrm{GeV}^{-2})$	$b_0[M^2 \leq 16\ \mathrm{GeV}^2]\ (\mathrm{GeV}^{-2})$	$b'\ (\mathrm{GeV}^{-2})$	γ
	7.4±1.0	20.0±3.0	12.0±2.0	1.0±0.2
	D/b_0 (mb)	D/b_0 (mb)		
	0.72±0.05	1.88±0.10		

The reason for obtaining a larger single diffraction cross section by using form (8) in place of (3) can be traced to the steeper than $1/M^2$ dependence of the differential cross section in the data, coupled to the fact that the diffractive peak in the low mass region ($x \simeq 1$) is smeared by resolution. Fitting the large mass data with (8) forces more events to be considered as belonging to the *low mass* ($M^2 \leq 6$ GeV^2) region, where the efficiency $E(M^2)$ is low (see Fig. 12). The efficiency correction, which is 1.47 averaging over all *low masses*, produces an artificially higher cross section in this mass region.

A quantitative argument that definitely favours the form (3)+(4) over (8)+(4) is based upon the observed track multiplicity distributions. At $\sqrt{s}$=546, within the region $(1-x) \leq 0.04$, we expect 27% or 48% of the events to be in the *low mass* region depending on whether we use our fit (3)+(4) or the fit (8)+(4). Since lower masses have lower multiplicities, the fraction of *low mass* events in the region $(1-x) \leq 0.04$ can be extracted from the track multiplicity distribution. Fig. 16a shows the multiplicity distribution of tracks observed in the FTF and/or S5 for events with $(1-x) \leq 0.04$ and no tracks in the VTPC. The multiplicity distribution for simulated events in the region of $(1\text{-}x) \leq 0.04$ with no tracks in the VTPC is shown in Fig. 16b for masses below and above 6 GeV^2. By fitting the two simulated shapes to the data, the *low mass* fraction is estimated to be 23±3%.

An additional way of determining this fraction is offered by the observation that, ac-

cording to our simulation, *low mass* events never have tracks in the VTPC. On the contrary, 28% of the simulated events with $M^2 > 6$ GeV^2 and $(1-x) \leq 0.04$ have tracks in the VTPC. In the data, out of 2723 events at $(1-x) \leq 0.04$, 545 events have one or more tracks in the VTPC, reflecting a *low mass* contribution of 28±3.5%. The average of the two numbers, the first one derived by fitting the multiplicity distribution and the second by using the pseudorapidity distribution, is 25±3%, in agreement with the value 27% from our fit (3)+(4).

VI. CONCLUSIONS

We have measured the single diffraction dissociation differential cross section for $\bar{p}p \rightarrow \bar{p}$ X at $\sqrt{s}$=546 and 1800 GeV and compared our results to theoretical expectations based on a supercritical Pomeron with a linear trajectory $\alpha(t) = 1 + \epsilon + \alpha' t$. The measured t-distributions are consistent with a slope $b = b_0 + 2\alpha' \ln(s/M^2)$, using the values α'=0.25 GeV^{-2} and b_0=6.5±2.0 GeV^{-2}. Fitting the measured M^2-distribution with the form $1/(M^2)^{1+\epsilon}$, we obtained $\epsilon = 0.155^{+0.014}_{-0.013} \pm 0.013$syst ($0.116^{+0.034}_{-0.026} \pm 0.013$ syst) at $\sqrt{s}$=546 (1800) GeV. The more accurate value of ϵ at $\sqrt{s}$=546 is somewhat higher than the value of ϵ=0.115±0.013 obtained from the rise of our total cross section in this energy region, suggesting that screening corrections should be included in the triple-Pomeron Regge model. The need for such corrections is strongly expressed by the s-dependence of the single diffraction total cross section, which exhibits a flat s-dependence instead of the $s^{2\epsilon}$ behaviour expected by the model.

ACKNOWLEDGEMENTS

We thank the Fermilab Accelerator Division for the construction and operation of the Tevatron and of the Antiproton Source. In particular, we feel indebted to Craig McClure, who interfaced our spectrometer hardware to the accelerator control system, and to D. Finley and H. Jostlein for many useful suggestions. We wish to thank the Fermilab Computer Division, the technical staff of CDF and the collaborating Institutions for their contribution to the construction and operation of CDF. The dedicated effort of the many technicians and engineers at Frascati and Rockefeller, who contributed to the design, construction and installation of the spectrometer and of the forward tracking vertex detectors, is warmly acknowledged; we especially thank M. Biagioli, G. Bisogni, A. Ceccarelli, M. DiVirgilio, G. Fontana, R. Heidecker, D. Humbert, E. Iacuessa, P. Locchi, A. Rutili, G. Sensolini, D. Scepanovich and M. Troiani. We are grateful to G. Tonelli and E. Focardi who led the construction of our silicon detectors. A very special thanks is due to our friends and colleagues R. Castaldi, C. Vannini and G. Sanguinetti, who made available to us most of the UA4 drift chambers (FTF and FTB), patiently introduced us to their reconstruction code and over several years have been helpful through many useful discussions. This work was supported by the Department of Energy, the National Science Foundation, the Istituto Nazionale di Fisica Nucleare and the Ministry of Science, Culture and Education of Japan.

References

[1] The CDF Collaboration, "Measurement of Small Angle Proton-Antiproton Elastic Scattering at $\sqrt{s} = 546$ and 1800 GeV".

[2] The CDF collaboration, "Measurement of the Total Proton-Antiproton Cross Section at $\sqrt{s} = 546$ and 1800 GeV".

[3] The CDF Collaboration, "The CDF Detector: An Overview", NIM A271 (1988) 387

The CDF Collaboration, "The CDF Vertex Time Projection Chamber System", NIM A268 (1988) 75

[4] K. Goulianos, "Diffractive Interactions of Hadrons at High Energies", Phys. Rep. 101 (1983) 169

[5] G. Alberi and G. Goggi, "Diffraction of Subnuclear Waves", Phys. Rep. 74 (1981) 1

[6] K.Goulianos, "A New Statistical Description of Hadronic and e^+e^- Multiplicity Distributions", Phys. Lett. B 193 (1987) 151

[7] L.Angelini, L.Nitti, M.Pellicoro and G.Preparata, "Some Aspects of the Structure of pp ($p\bar{p}$) Scattering at High Energy", Phys. Rev. D 41 (1990) 2081

[8] R.D. Field and G.C.Fox, "Triple Regge and Finite Mass Sum Rule Analysis of the Inclusive Reaction $pp \rightarrow pX$", Nucl.Phys. B80 (1974) 367

[9] D.P.Roy and R.G.Roberts, "Triple Regge Analysis of $pp \rightarrow pX$ and Some Related Phenomena - A Detailed Study", Nucl. Phys. B77 (1974) 240

[10] A.Donnachie and P.V.Landshoff, "Multi-gluon Exchange in pp Elastic Scattering", Phys. Lett. 123B (1983) 345

[11] P.D.B.Collins and F.Gault, "Large-$|t|$ pp, $p\bar{p}$ Elastic Scattering and the Triple-Scattering Mechanism", Phys. Lett. 112B (1982) 255.

[12] A. Capella, J. Tran Thanh Van and J. Kwiecinski, "Minijets, QCD and Unitarity", Phys. Rev. Lett. 58 (1987) 2015

[13] Y.Akimov et al., "Analysis of Diffractive pd→Xd and pp→Xp Interactions and Test of the Finite-Mass Sum Rule", Phys. Rev. D14 (1976) 3148

[14] Y.Akimov et al.," Excitation of High Energy Protons into Low Mass States in p-d Interactions", Phys. Rev. Lett. 35 (1975) 763

[15] E.Gotsman, E.M.Levin and U.Maor, "Diffractive Dissociation and Large Rapidity Gaps in $p\bar{p}$ Collisions", FNAL Report 93-000 (1993)

[16] R.L.Cool, K.Goulianos, S.L.Segler, H.Sticker and S.N.White, "Diffraction Dissociation of $\pi^{\pm}$, $K^{\pm}$ and $p^{\pm}$ at 100 and 200 GeV/c", Phys. Rev. Lett. 47 (1981) 701

[17] J.C.Armitage et al., "Diffraction Dissociation in Proton-Proton Collisions at ISR Energies", Nucl. Phys. B194 (1982) 365

[18] M.G.Albrow et al., "Inelastic Diffractive Scattering at the ISR", Nucl. Phys. B108 (1976) 1

[19] R. Engel, F.W.Bopp, D.Pattermann and J.Ranft, " Extrapolation of Hadron Cross Sections to Supercollider Energies within the Two Component Parton Model ", Phys. Rev. D46 (1992) 5192

[20] P. Aurenche, A.Cappella, J.Kwiecinski, M.Maire, J.Ranft and J.Tran Thanh Van, "Multiparticle Production in a Two-Component Dual Parton Model", Phys. Rev. D45 (1992) 92

[21] D.Bernard et al., The UA4 Collaboration, "The Cross Section of Diffraction Dissociation at the CERN SPS Collider", Phys. Lett. B186 (1987) 227

Table 1: Analysis event flow

	$\sqrt{s}$=546	1^{st} run at $\sqrt{s}$=1800	2^{nd} run at $\sqrt{s}$=1800
	no. of events	no. of events	no. of events
Triggers	15272	16303	57177
TOF FILTER	13129	8851	15794
VTPC FILTER	12683	7813	13777
HITS CUT	12058	6884	10561
S1*S2 TRACK CUT	10462	6093	9192
FIDUCIAL CUT 1+2+3	5643	1417	3194
VERTEX CUT	4906	1090	2616
Background removal	4906	1070	2616
A(x,t)> 0.02	4873	1065	2609
Loss corrections			
VTPC+TOF FILTER	1.011±0.004	1.019±0.002	1.018±0.008
Nuclear interactions	1.024±0.002	1.024±0.002	1.024±0.002
Prescaling factor ×2	1.84×2	1.8×2	1× 2

Table 2: Fit results

	$\sqrt{s}$=546 GeV	$\sqrt{s}$=1800 GeV
$\int\int_{A(x,t)\geq 0.02} \frac{N_{ev}(M^2,t)}{A(M^2,t)} dM^2 dt$	120213± 1752	35760±656
$\int\int_{A(x,t)\geq 0.02} L \cdot \frac{d^2[\sigma_{sd}+\sigma_{nd}]}{dM^2 dt} dM^2 dt$	119268	34919
$L \cdot \sigma_{sd} = \int_{1.4GeV^2}^{0.15s} dM^2 \int_0^\infty L \cdot \frac{d^2\sigma_{sd}}{dM^2 dt} dt$	160282±7537	34551 ±3382
$L \cdot \sigma_{nd} = \int_{1.4GeV^2}^{0.15s} dM^2 \int_0^\infty L \cdot \frac{d^2\sigma_{nd}}{dM^2 dt} dt$	30764 ±2728	10913±2168
L (luminosity, mb^{-1}) [2]	20625±2.1%	3939±3.3%
σ_{sd} (mb)	7.8±0.3	8.8±0.7
$D = G(0) \cdot (s/s_0)^\epsilon$ (mb/GeV^{-2})	2.90±0.36	2.44±0.50
ϵ	$0.155^{+0.014}_{-0.013}$	$0.116^{+0.034}_{-0.026}$
b_0 (GeV^{-2})	8.7±0.6	5.5±0.6
σ_{nd} (mb)	1.50±0.13	2.8±0.5
b' (GeV^{-2})	9.0±1.2	7.6±1.0
γ	0.46±0.18	0.12±0.20

Table 3: Fit parameter correlation matrix

	b_0	I	b'	γ	ϵ
D	0.17	-0.74	0.08	0.66	-0.95
b_0		0.04	-0.3	-0.09	0.2
I			-0.17	-0.97	0.75
b'				0.33	-0.15
γ					0.69

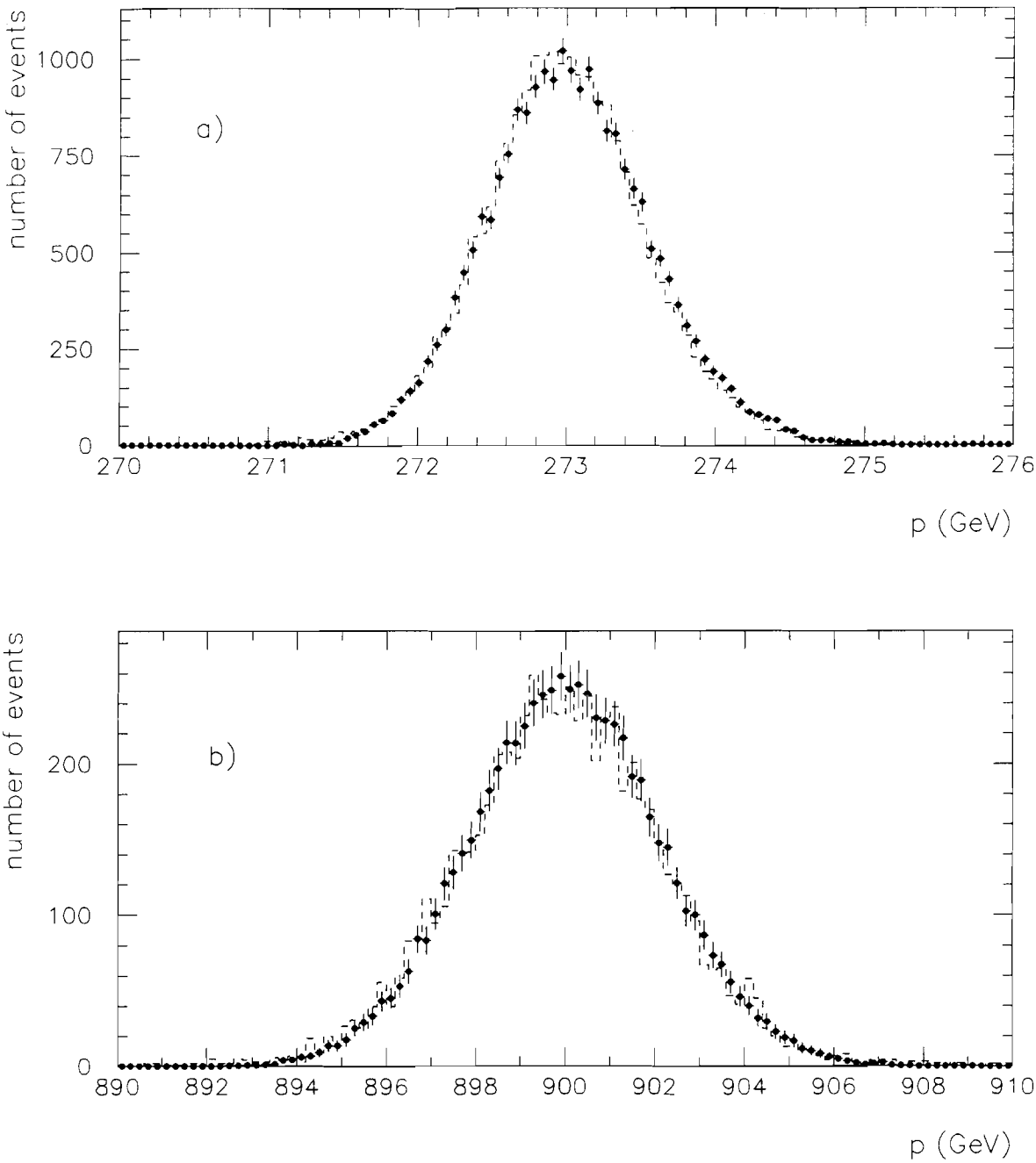

Figure 1: Reconstructed momentum distribution of elastic events at (a) $\sqrt{s}$ = 546 and (b) $\sqrt{s}$=1800: (•) data; (– – –) simulation.

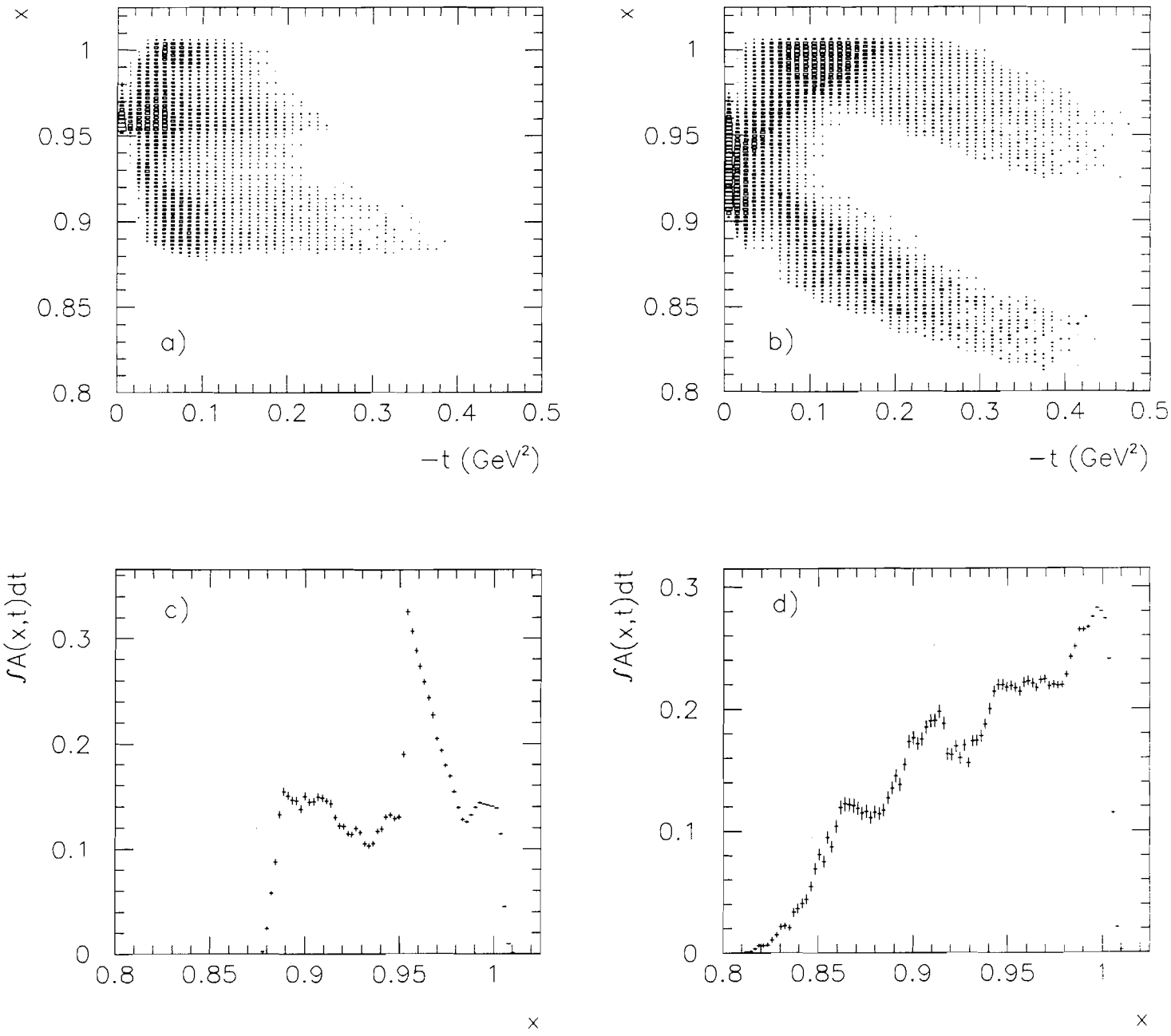

Figure 2: Spectrometer acceptance $A(x,t)$ at (a) $\sqrt{s}$=546 and (b) $\sqrt{s}$=1800. Integrated acceptance $\int_0^{0.5} A(x,t)dt$ at (c) $\sqrt{s}$=546 and (d) $\sqrt{s}$=1800.

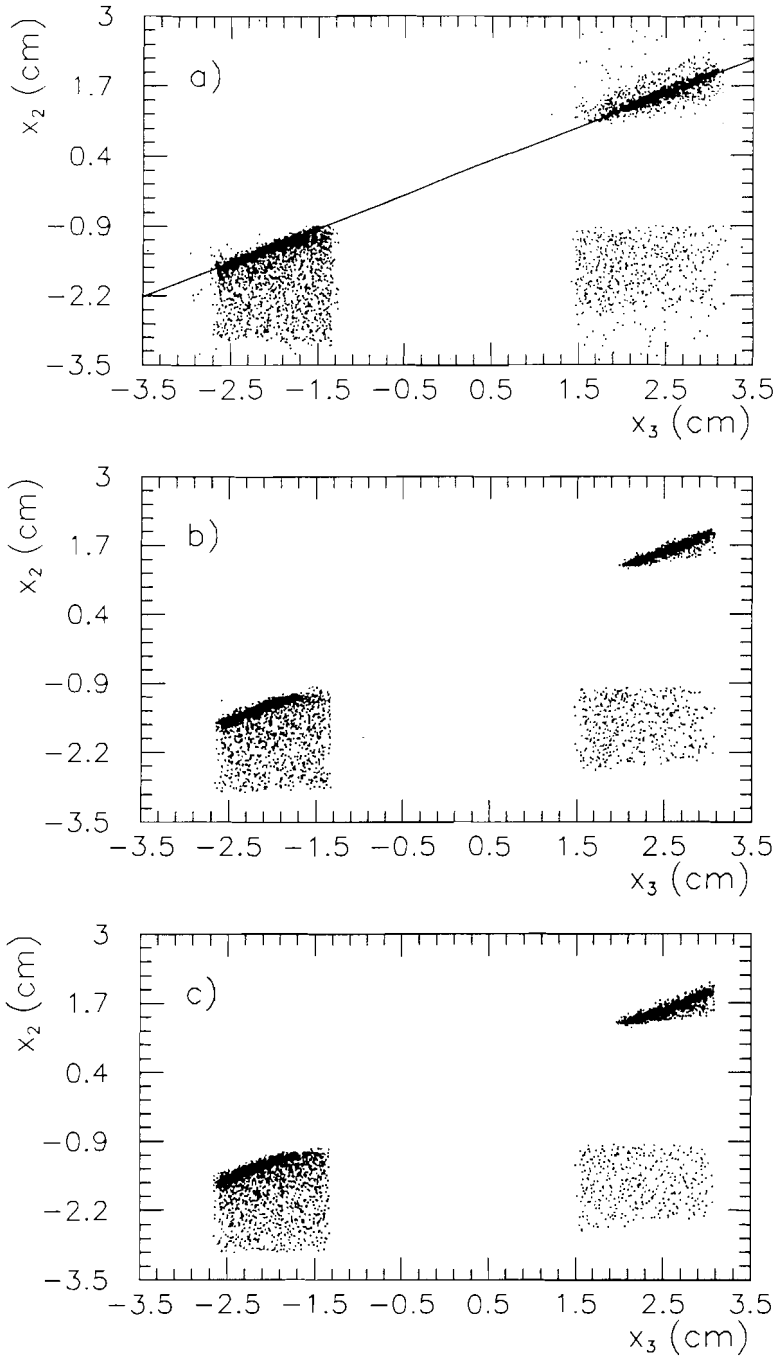

Figure 3: Distribution of antiproton x_2 vs x_3 coordinates at $\sqrt{s}$=546 (the S2 and S3 detectors are separated by a string of dipole magnets): (a) all events; (b) events which pass all cuts listed in Table 1; (c) simulated events.

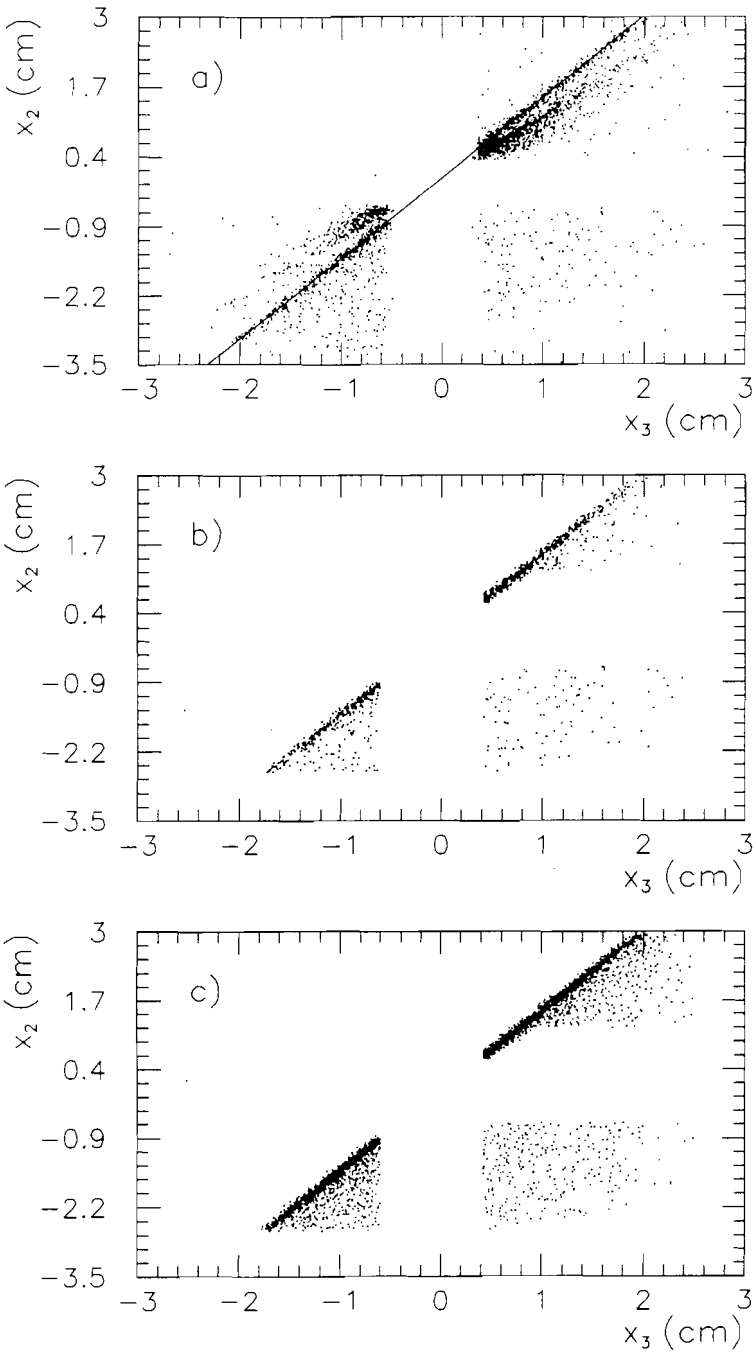

Figure 4: Distribution of x_2 vs x_3 coordinates at $\sqrt{s}$=1800: (a) all events; (b) events which pass all cuts listed in Table 1; (c) simulated events.

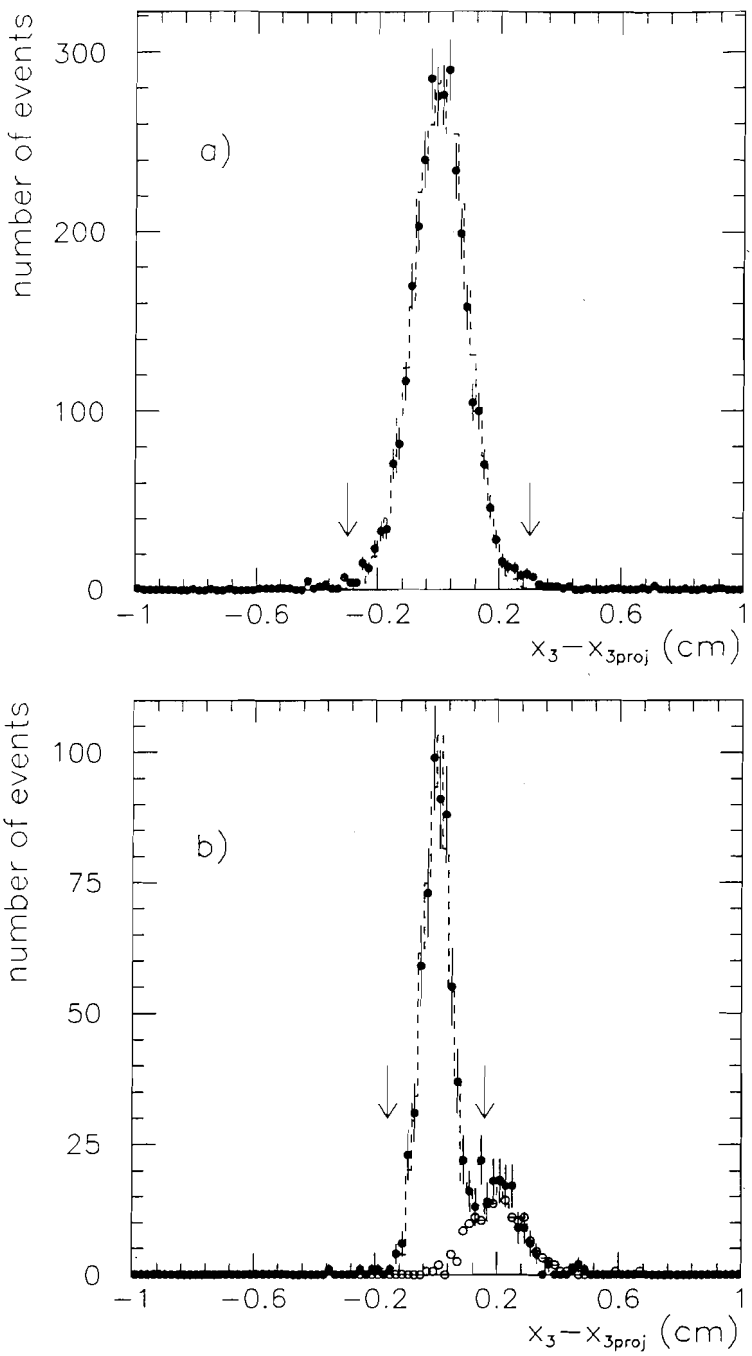

Figure 5: (a) Distribution of x_3-x_{3proj} at $\sqrt{s}$=546, where x_3 is the x-coordinate measured by S3 and x_{3proj} is the position in S3 evaluated by using S1, S2 and assuming x=y=0 at z=0: (•) data; (− − −) simulation. The arrows mark the position of the FIDUCIAL CUT 2 (see text).
(b) Distribution of x_3-x_{3proj} at $\sqrt{s}$=1800: (•) data; (○) identified beam halo normalized to the data at x_3-x_{3proj} ≥0.2 cm; (− − −) sum of the normalized halo and of the complementary amount of simulated events.

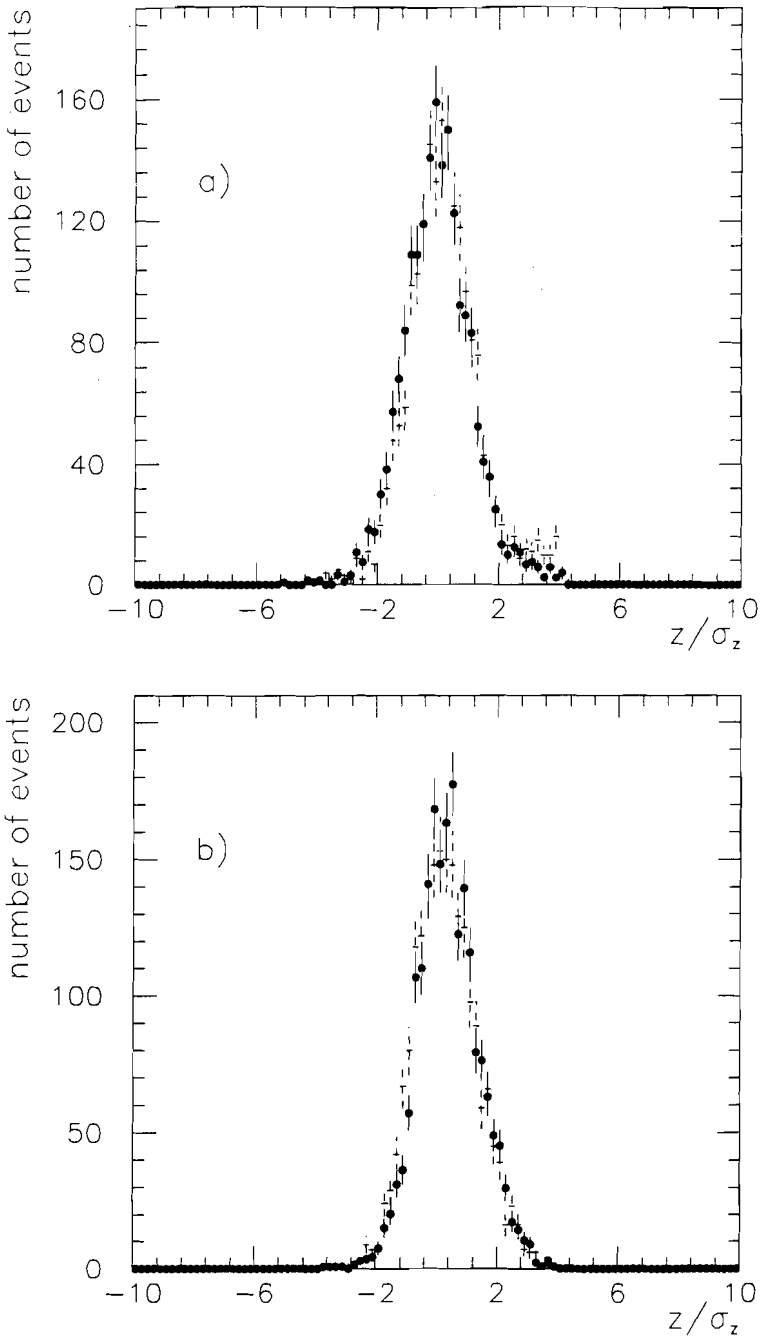

Figure 6: Vertex z-distributions measured at $\sqrt{s}$=546.
(a) Vertex measured by the VTPC in units of the spread σ_z of the interaction region ($\simeq$ 30 cm). The vertex reconstruction accuracy of the VTPC is $\simeq \pm 1$ cm. Data (•) and simulated events (− − −) are filtered as described in Table 1.
(b) Vertex measured by the FTF and/or S5 detectors for events with no tracks in the VTPC in units of σ_z convoluted with the reconstruction error for each vertex ($\simeq \pm 10$ cm): (•) data; (− − −) simulation.
The asymmetry in the z-distributions for data and simulated events is caused by secondary interactions.

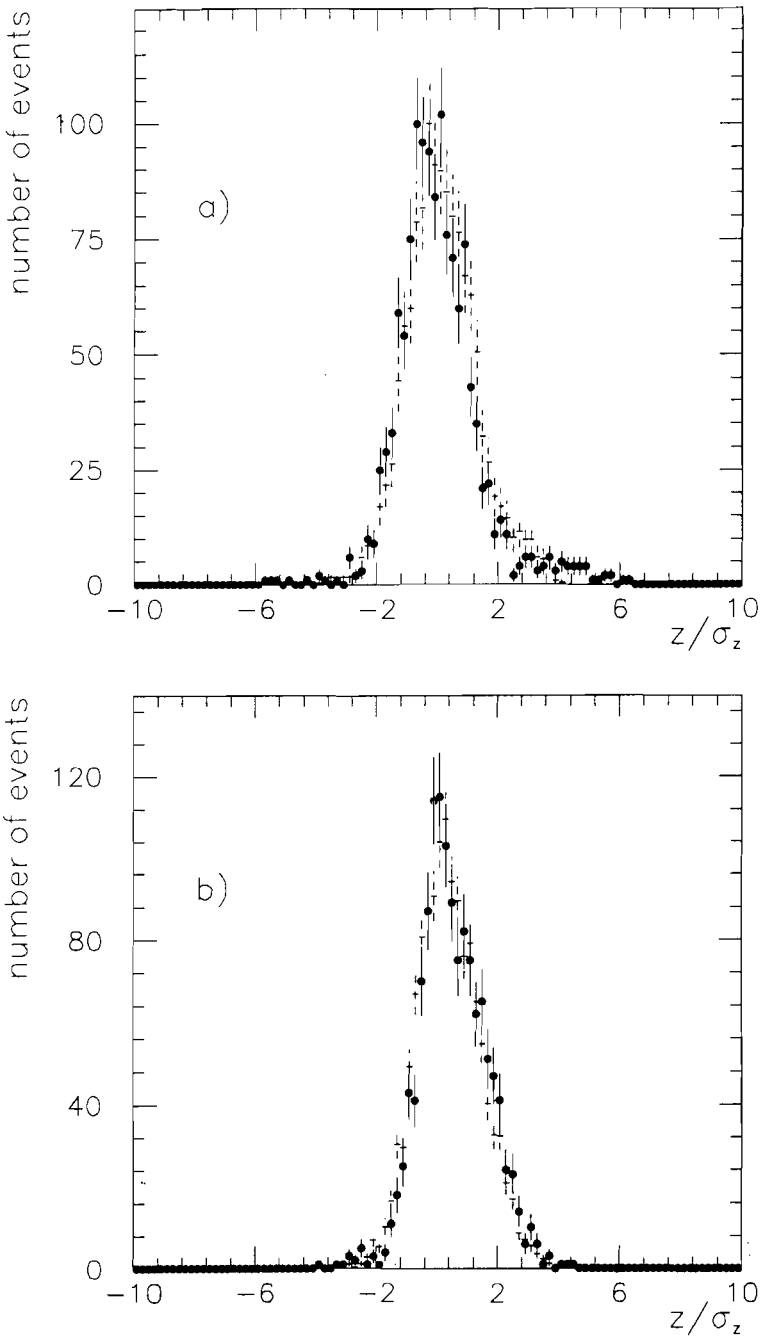

Figure 7: Vertex z-distributions at $\sqrt{s}$=1800.
(a) Vertex measured by the VTPC. (b) Vertex measured by the FTF and/or S5 detectors for events with no tracks in the VTPC: (•) data; (− − −) simulation.

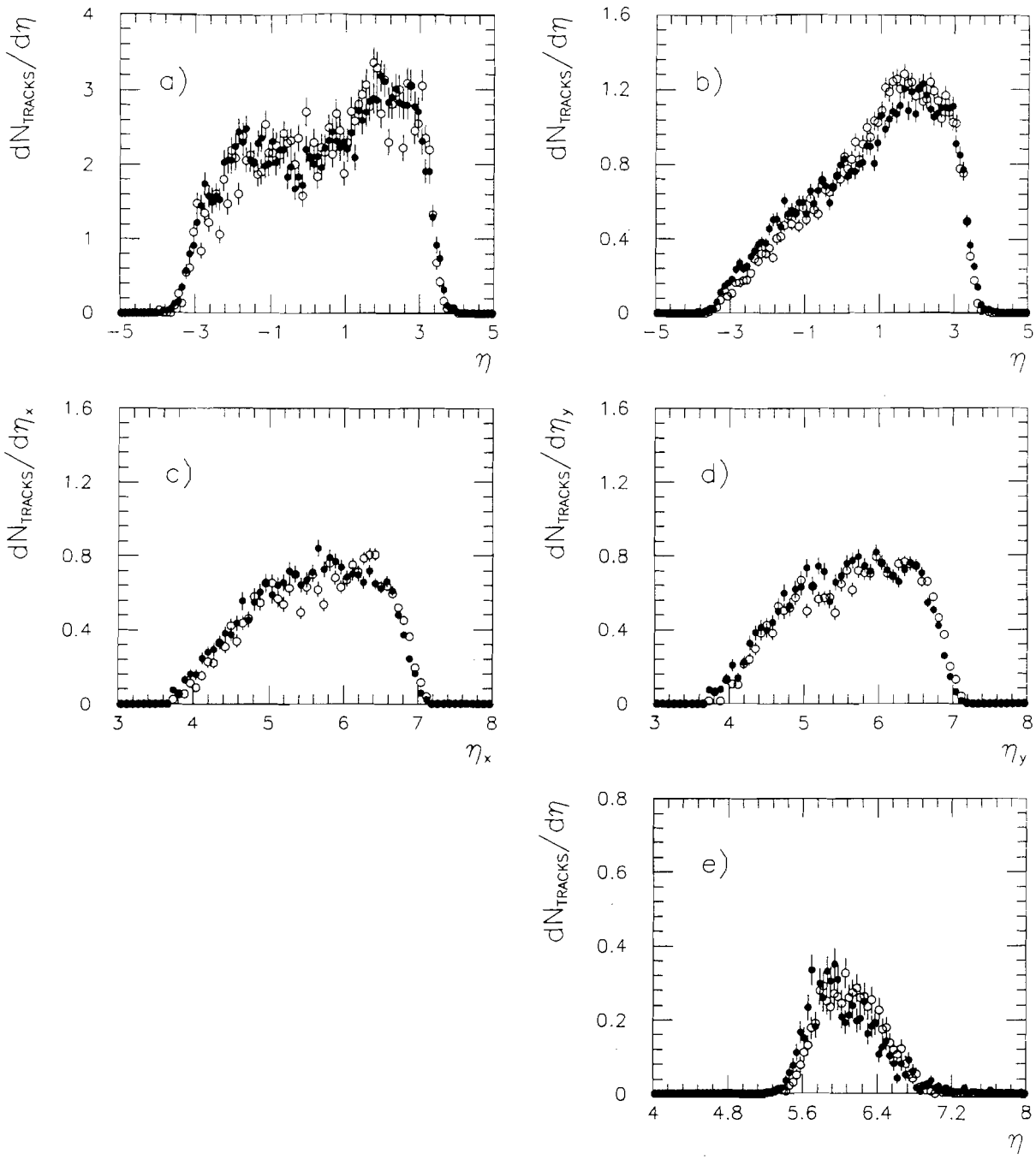

Figure 8: Pseudo-rapidity distributions as measured by the different vertex detectors at $\sqrt{s}$=546. Data (•) are not corrected for the detector acceptance. The simulation (○) is normalized to the total number of measured tracks.
(a) η-distribution of tracks detected by the VTPC for events with $x \leq 0.95$.
(b) η-distribution of tracks detected by the VTPC for events with $x > 0.95$.
(c,d) η_x and η_y-distributions measured by the FTF for all events. The angles θ_x and θ_y are measured independently and $\eta_{x(y)} = -\ln(\tan\frac{\theta_{x(y)}}{2})$
(e) η-distribution measured by S5 for all events.

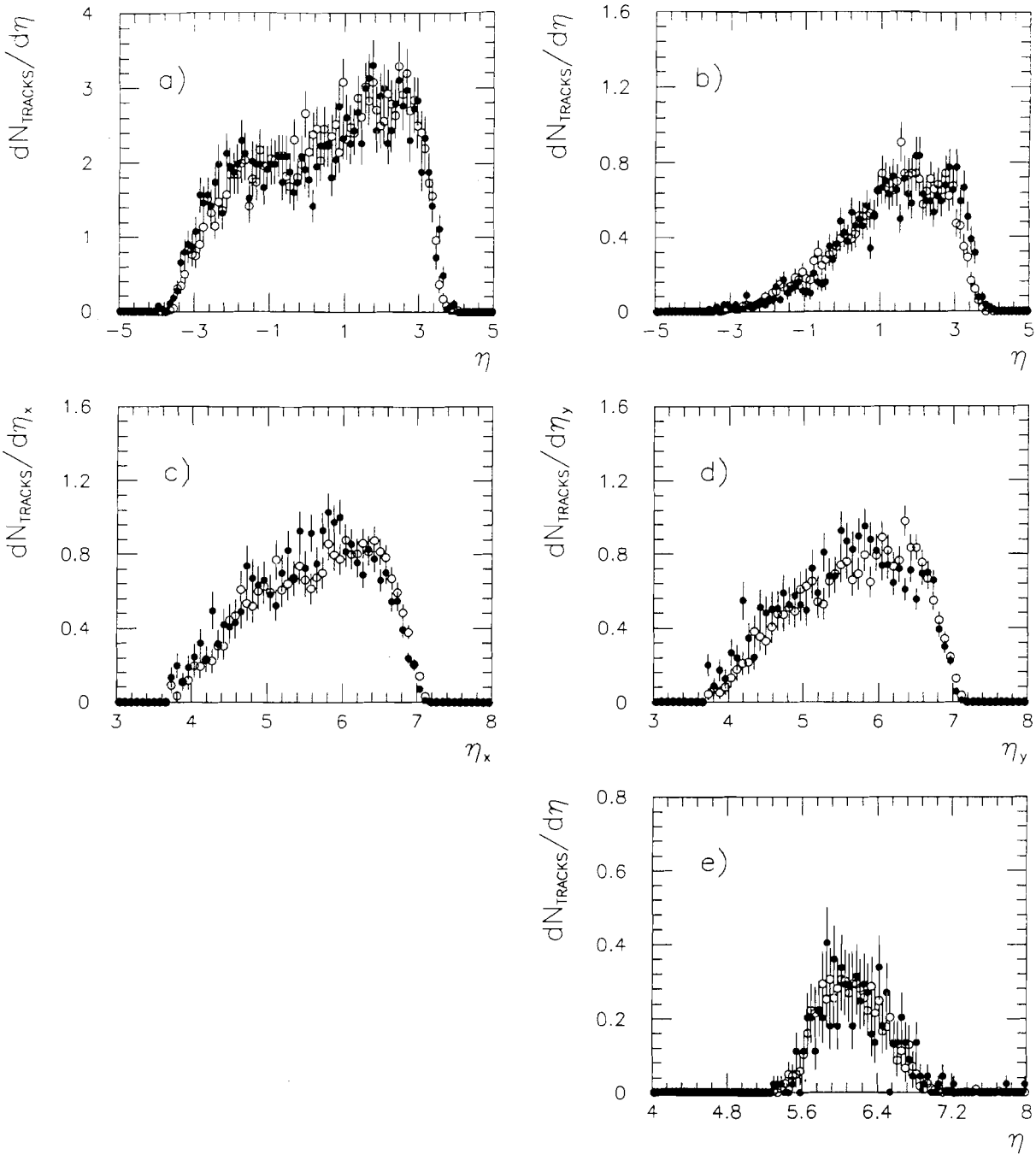

Figure 9: Pseudo-rapidity distributions as measured by the different vertex detectors at $\sqrt{s}$=1800. Data (•) are not corrected for the detector acceptance. The simulation (○) is normalized to the total number of measured tracks.
(a) η-distribution of tracks detected by the VTPC for events with $x \leq 0.995$.
(b) η-distribution of tracks detected by the VTPC for events with $x > 0.995$.
(c,d) η_x and η_y-distributions measured by the FTF for all events.
(e) η-distribution measured by S5 for all events.

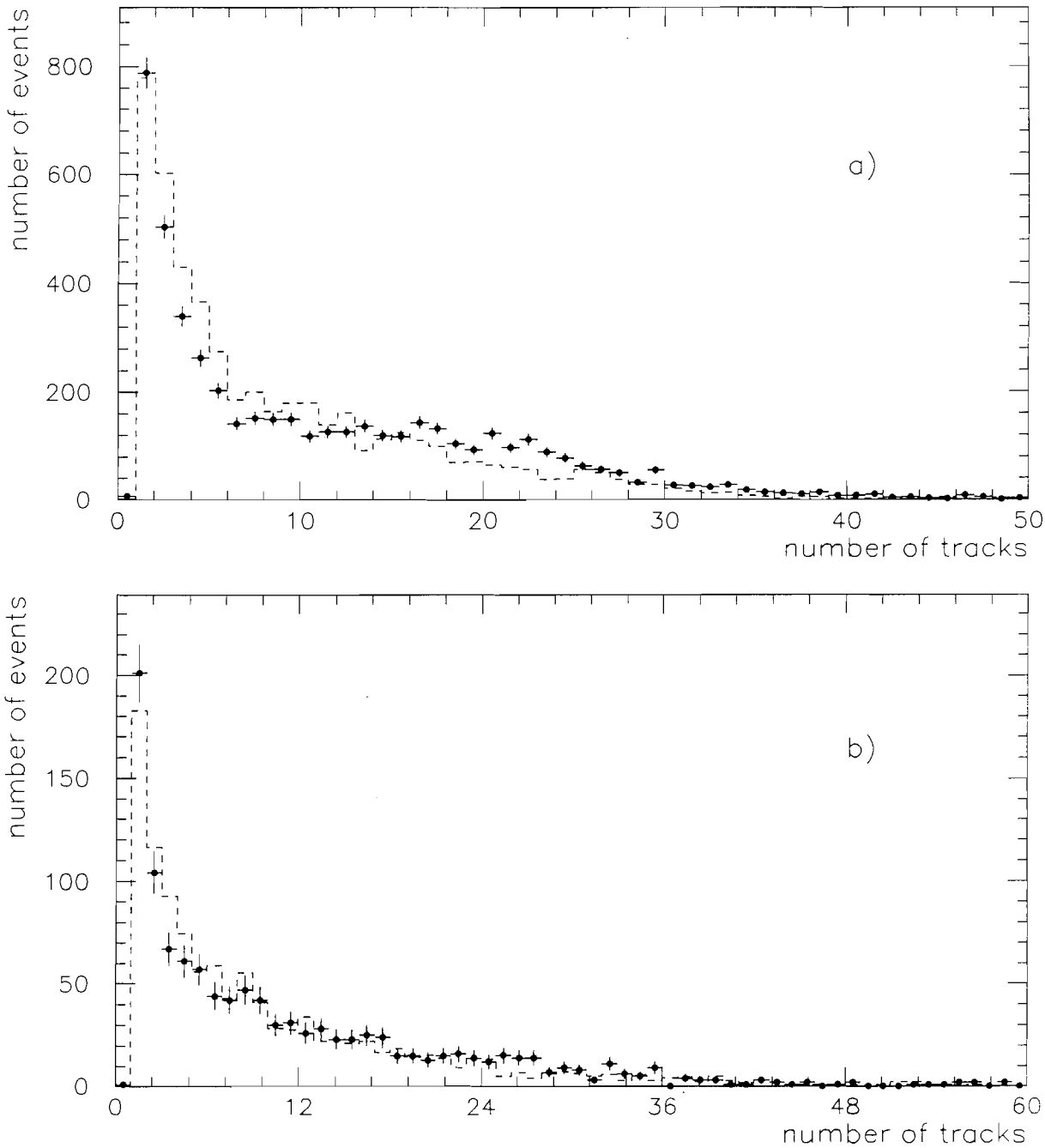

Figure 10: Multiplicity distributions of tracks measured in all detectors. Data (•) and simulation (– – –) are compared at (a) $\sqrt{s}$=546 and (b) $\sqrt{s}$=1800.

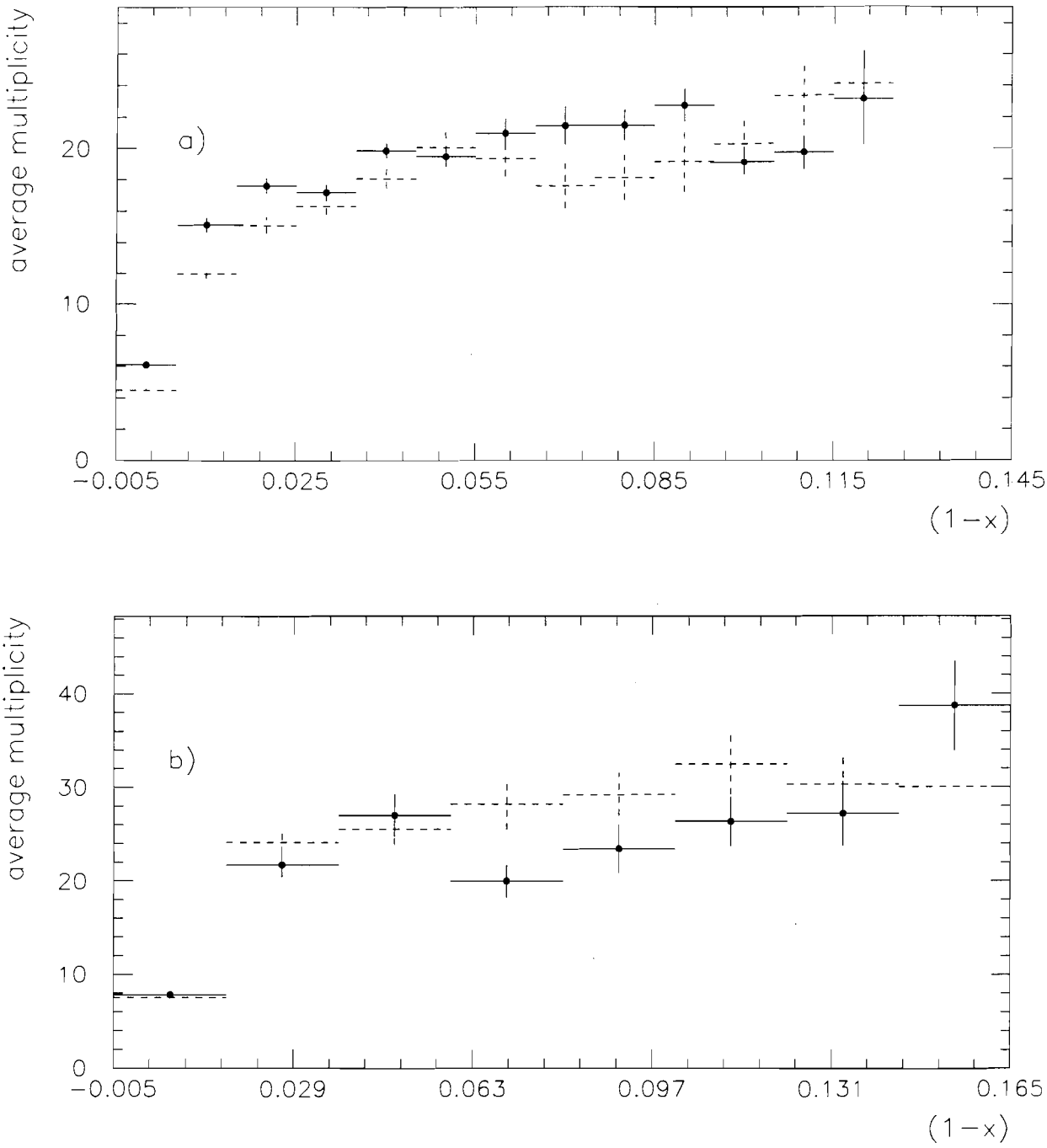

Figure 11: Average number of tracks in all vertex detectors as a function of $(1-x)$. Data (•) and simulation (− − −) are compared at (a) $\sqrt{s}$=546 and (b) $\sqrt{s}$=1800.

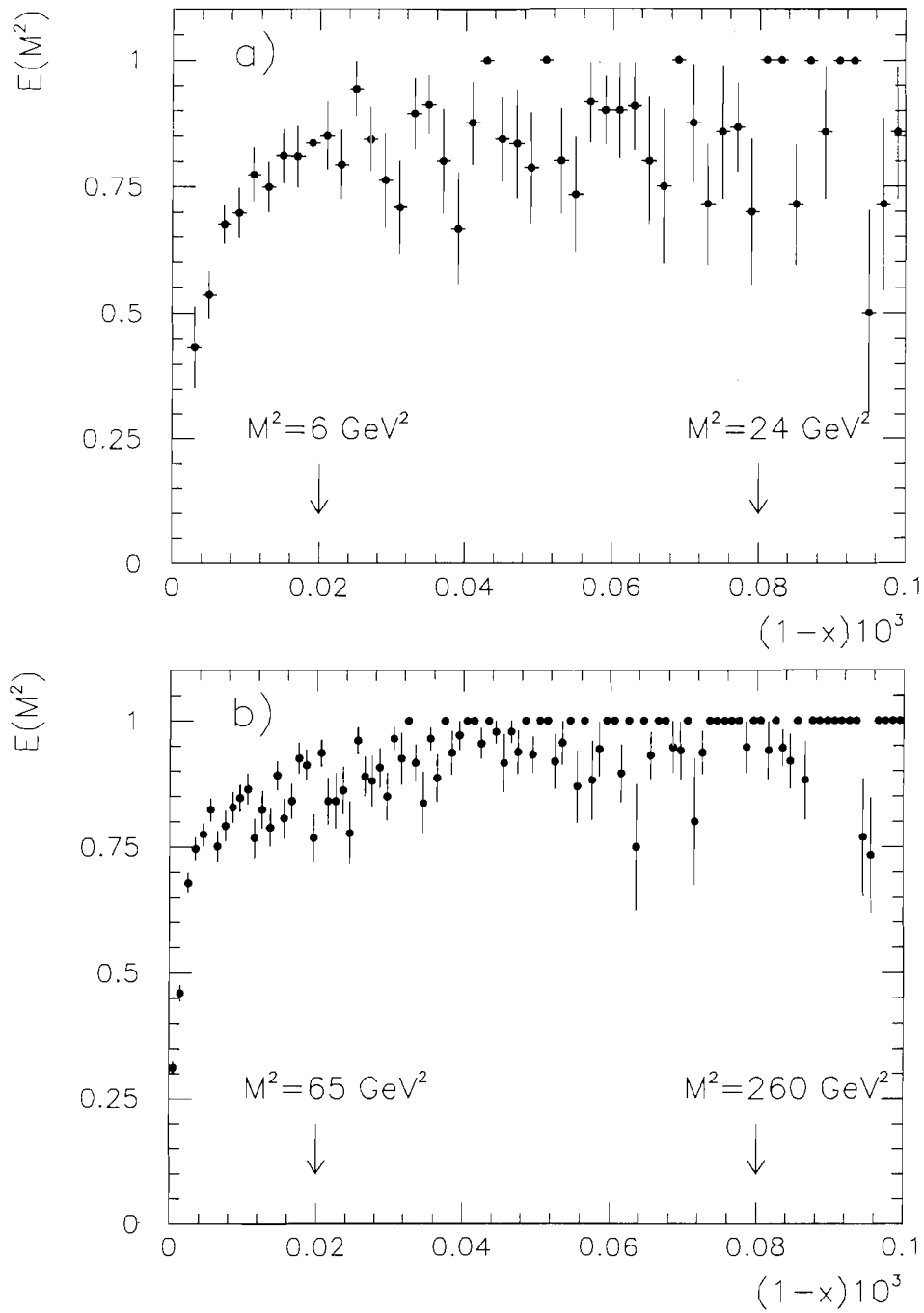

Figure 12: Efficiency $E(M^2)$ for triggering on a diffractive cluster and reconstructing its vertex as a function of $1 - x = M^2/s = (p_0\text{-}p)/p_0$, where p is the recoil antiproton momentum. $E(M^2)$ is determined by our simulation at (a) $\sqrt{s}$=546 and (b) $\sqrt{s}$=1800.

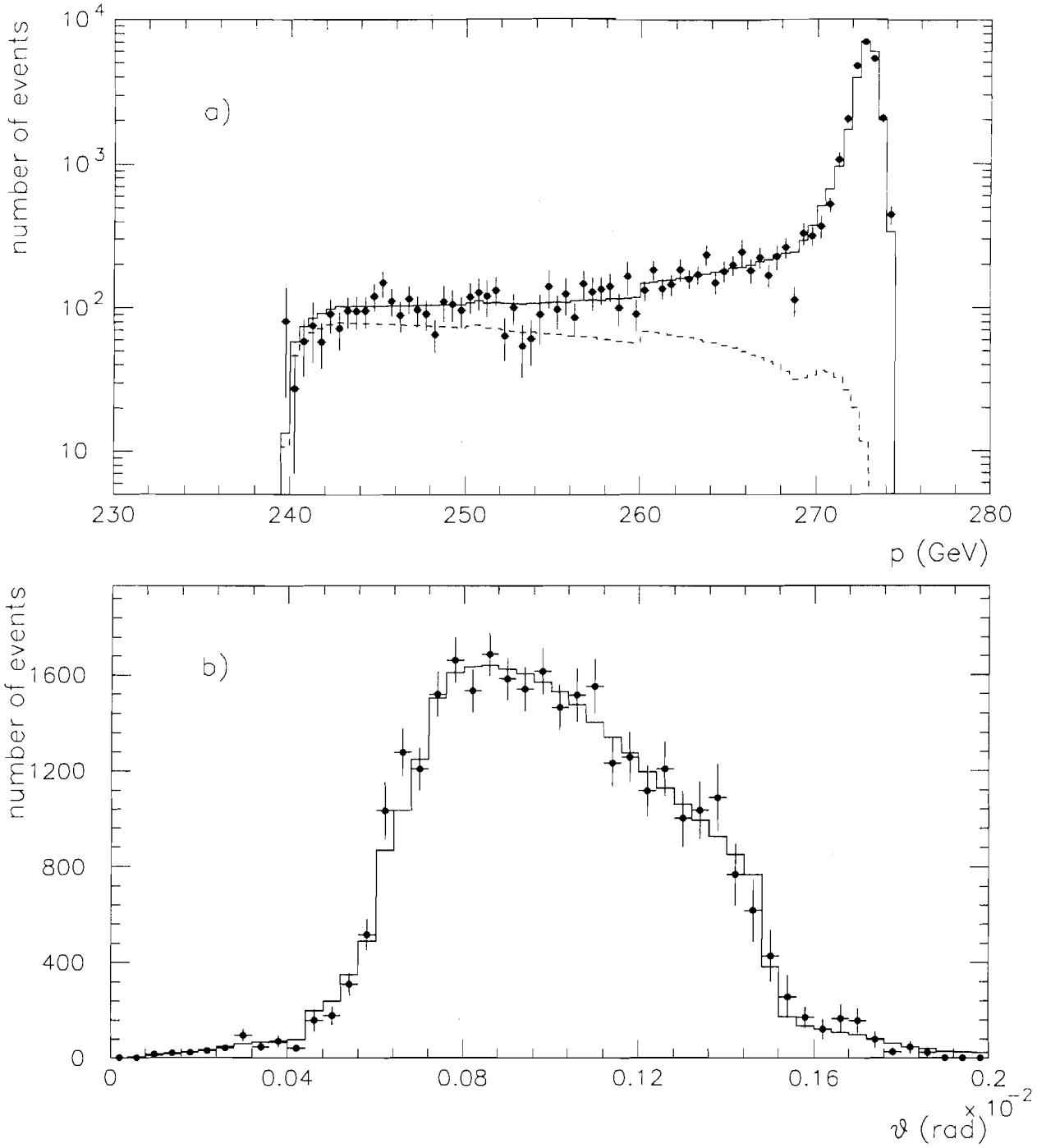

Figure 13: (a) Momentum distribution for all events at $\sqrt{s}$=546. The data (•) are corrected for the spectrometer acceptance A; the solid line represents our fit with form (3)+(4) (see Sec. IV); the dashed line is the non-diffractive contribution (4). In our fit the data were arranged in a θ-p matrix with cells $\Delta\theta \cdot \Delta$p=40·0.5 μrad·GeV. The momentum distribution shown was obtained by integrating over the spectrometer angular acceptance.
(b) Angular distribution for all events at $\sqrt{s}$=546, after integrating over the spectrometer momentum acceptance. Data (•) are corrected for the acceptance A; the solid line represents the fit (3)+(4).

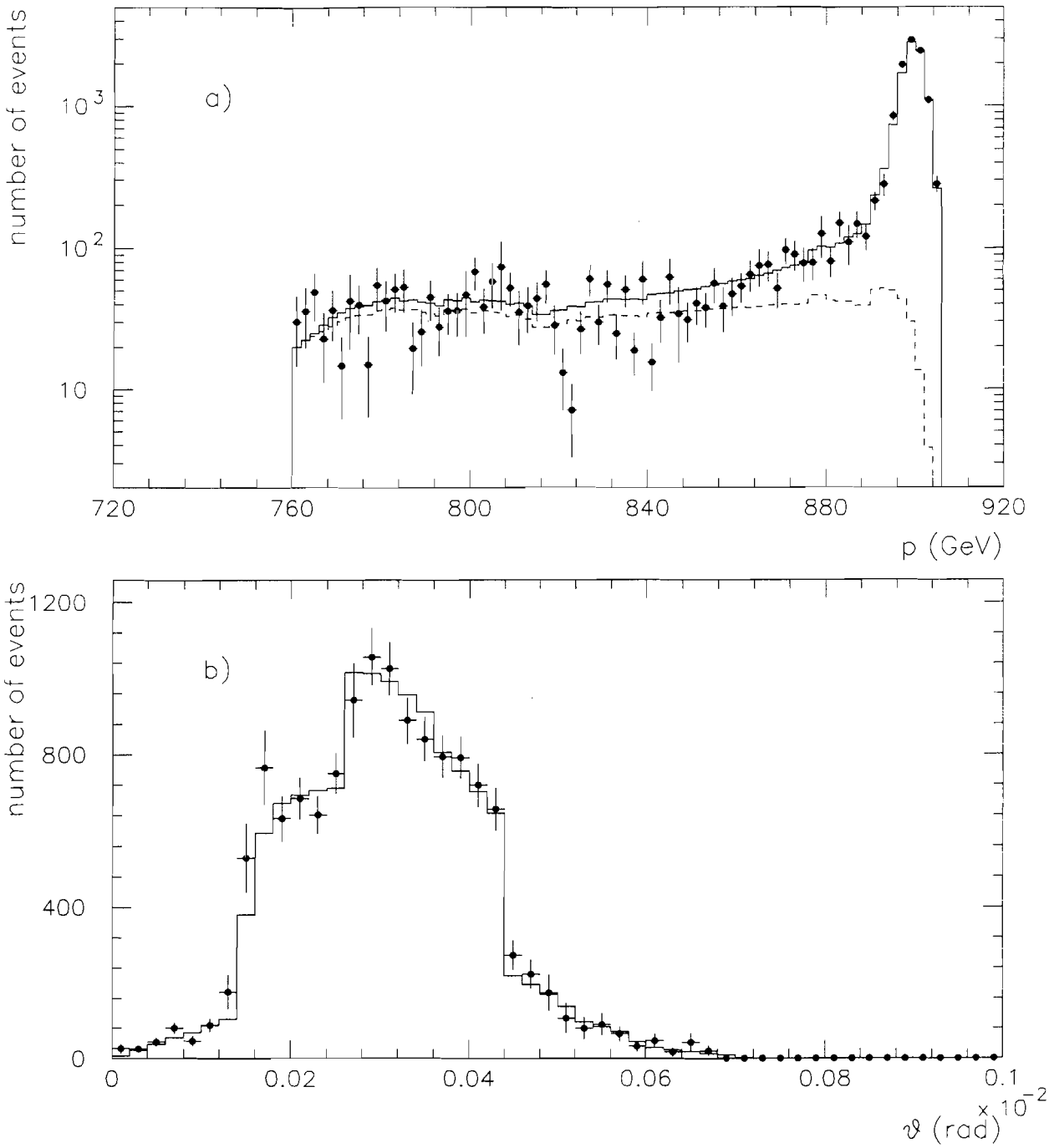

Figure 14: (a) Momentum and (b) production angle distributions at $\sqrt{s}$=1800. At this energy, the data (•) were arranged in a mesh $\Delta\theta \cdot \Delta$p=20·2.0 μrad·GeV. The solid line represent our fit (3)+(4); the dashed line is the non-diffractive contribution (4).

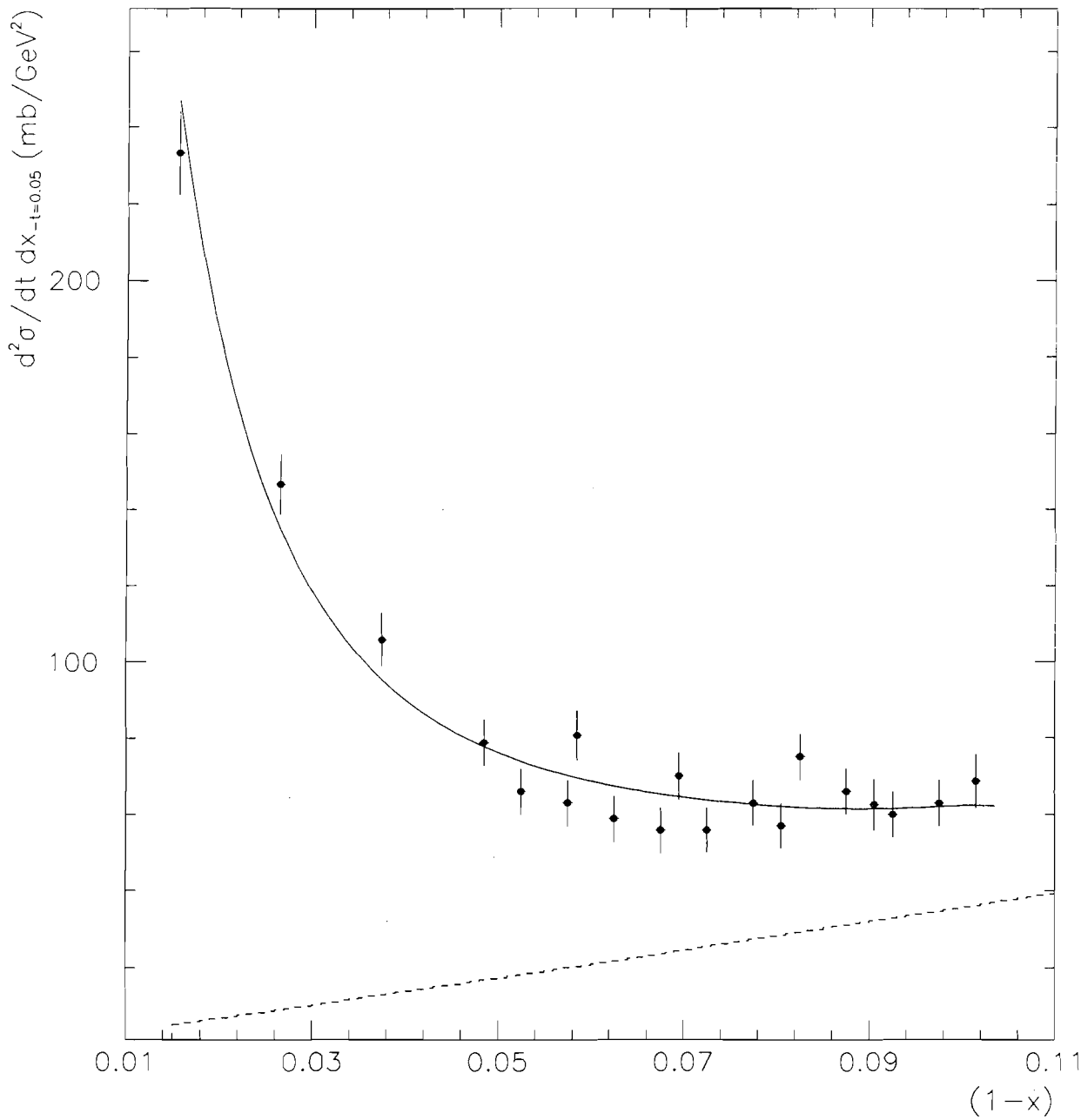

Figure 15: (1-x) distribution of data at $\sqrt{s}$=20 GeV from [16, 17]. The data (•) are at -t=0.05. The solid line is the fitted form (3)+(4); the dashed line is the non-diffractive contribution (4).

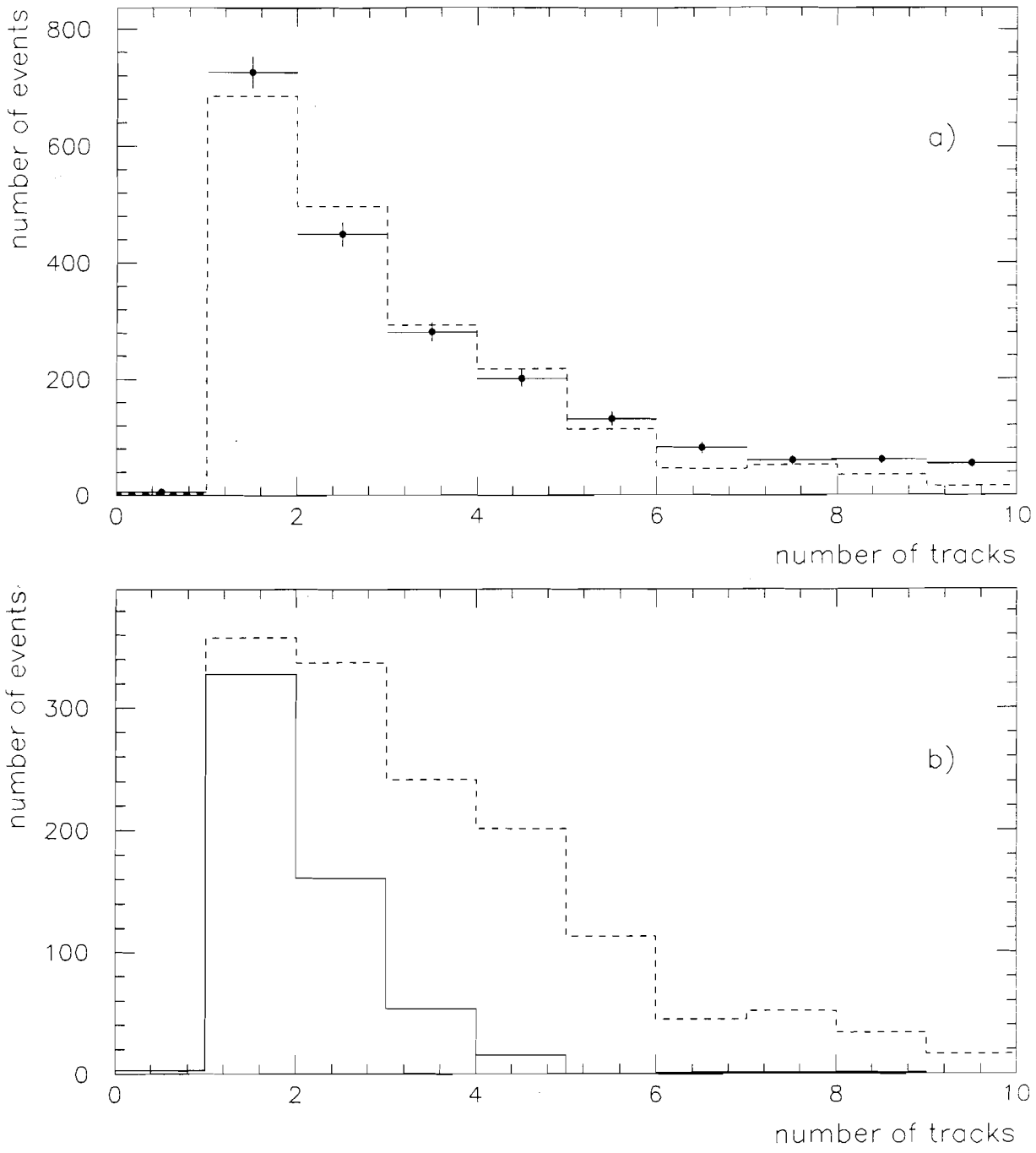

Figure 16: Distribution of the number of tracks at $\sqrt{s}$=546. (a) Tracks measured by the FTF+S5 detectors for events with $x \geq 0.996$ and no tracks in the VTPC: (•) data; (– – –) best fit using the shapes in (b).
(b) Tracks measured by the FTF+S5 detectors for simulated events with $x \geq 0.996$, no tracks in the VTPC and $M^2 \leq 6$ GeV^2 (solid line) or $M^2 > 6$ GeV^2 (dashed line).